APPENDIX E:
COMPARE COMPLETE FIELD TO GAUSSIAN APPROXIMATION

This appendix compares the complete velocity potential field for a focused source (i.e., complete field) to the three-dimensional Gaussian approximation in the focal region in order to determine the validity of the approximation. The comparison was done by first finding the velocity potential field for three ideally focused sources with f-numbers of 1, 2, and 4 and diameters of 5, 2.5, and 1.25 cm, respectively, at frequencies from 2 to 14 MHz in steps of 1 MHz. The field was calculated on a rectangular grid extending from 4 to 6 cm from the aperture plane of the source along the beam axis (focal length for all sources was ~ 5 cm) and radially 2 cm off of the beam axis using a grid spacing of 10 μm. The medium in which the field was calculated was lossless and had a sound speed of 1540 m/s. Then, the complete field was compared to the Gaussian approximation by calculating the percent difference as defined by

$$\%\,Difference = 100 \cdot \frac{\iiint_{V'} \left(\left(\frac{\phi_{comp}(\lambda)}{\max_{V'}\left(\phi_{comp}(\lambda_o)\right)} \right)^2 - e^{-2\left(\left(\frac{x'}{w_x(\lambda)}\right)^2 + \left(\frac{y'}{w_y(\lambda)}\right)^2 + \left(\frac{z'}{w_z(\lambda)}\right)^2 \right)} \right)^2 dx'dy'dz'}{\iiint_{V'} \left(\frac{\phi_{comp}(\lambda)}{\max_{V'}\left(\phi_{comp}(\lambda_o)\right)} \right)^4 dx'dy'dz'} \tag{E.1}$$

for each source at each frequency where λ_o was the wavelength corresponding to 8 MHz. Also, the "focus" at which the Gaussian approximation was centered (i.e., $x'=y'=z'=0$) was defined to be the location at which $\phi_{comp}(\lambda_o)$ was maximum for each source. The equivalent Gaussian dimensions for each source at each frequency were then given by,

$$\begin{aligned} w_x &= w_y = 0.87\lambda f\# \\ w_z &= 6.01\lambda\left(f\#\right)^2. \end{aligned} \tag{E.2}$$

The volume integral in Equation (E.1) was simplified before evaluating because the field is symmetric about the beam axis yielding

$$\%\,Difference = 100 \cdot \frac{\int_{-L/2}^{L/2}\int_{0}^{r_{max}} \left(\left(\frac{\phi_{comp}(\lambda)}{\max_{V'}\left(\phi_{comp}(\lambda_o)\right)} \right)^2 - e^{-2\left(\left(\frac{r'_\rho}{w_x(\lambda)}\right)^2 + \left(\frac{z'}{w_z(\lambda)}\right)^2 \right)} \right)^2 r'_\rho dr'_\rho dz'}{\int_{-L/2}^{L/2}\int_{0}^{r_{max}} \left(\frac{\phi_{comp}(\lambda)}{\max_{V'}\left(\phi_{comp}(\lambda_o)\right)} \right)^4 r'_\rho dr'_\rho dz'} \tag{E.3}$$

where the limits of integration were set by using a window length of L = 13 mm and $r_{max} = 12.5 \cdot 0.51\lambda(f\#)$ and $r'_\rho = \sqrt{x'^2 + y'^2}$. The double integral in Equation (E.3) was then evaluated using double integration function in Matlab based on the adaptive-recursive Newton-Cotes 8 panel rule where ϕ_{comp} values away from the grid points were linearly extrapolated from the closest grid values. In addition to calculating the percent difference according to Equation (E.3), the percent difference was also calculated from

$$\%\,Difference = 100 \cdot \frac{\int_{-L/2}^{L/2} \left(\left(\frac{\phi_{comp}(\lambda)}{\max_{V'}\left(\phi_{comp}(\lambda_o)\right)} \right)^2 - e^{-2\left(\frac{z'}{w_z(\lambda)}\right)^2} \right)^2 dz'}{\int_{-L/2}^{L/2} \left(\frac{\phi_{comp}(\lambda)}{\max_{V'}\left(\phi_{comp}(\lambda_o)\right)} \right)^4 dz'} \tag{E.4}$$

also using an L of 13 mm due to the importance of Gaussian approximation of the field along the beam axis in the equation for the generalized attenuation-compensation function presented in Chapter 2.

The percent differences from Equations (E.3) and (E.4) for all three sources at each frequency are given in Figure E.1. The percent difference calculated over the entire field is always less than 18.75%, indicating that assuming the velocity potential field is a three-dimensional Gaussian distribution is a reasonable approximation. However, before concluding, the differences between the complete and Gaussian fields were explored in greater detail. The percent differences calculated from Equations (E.3) and (E.4) both exhibit a large increase after a frequency of 8 MHz for the *f*/4 transducer. However, the percent differences from both equations for the *f*/1 transducer are relatively constant with frequency with the results from Equation (E.3) plateauing at ~18%. Likewise, the percent differences for the *f*/2 transducer as given by Equation (E.3) also seem to approach a plateau of ~18% while the percent differences from Equation (E.4) are relatively constant with frequency. Hence, the percent differences for

the *f*/4 transducer are probably related to errors in the approximation along the beam axis, *z*-axis, whereas the errors in the *f*/1 and *f*/2 transducers are probably more related to other errors in the approximation (i.e., possibly side lobes).

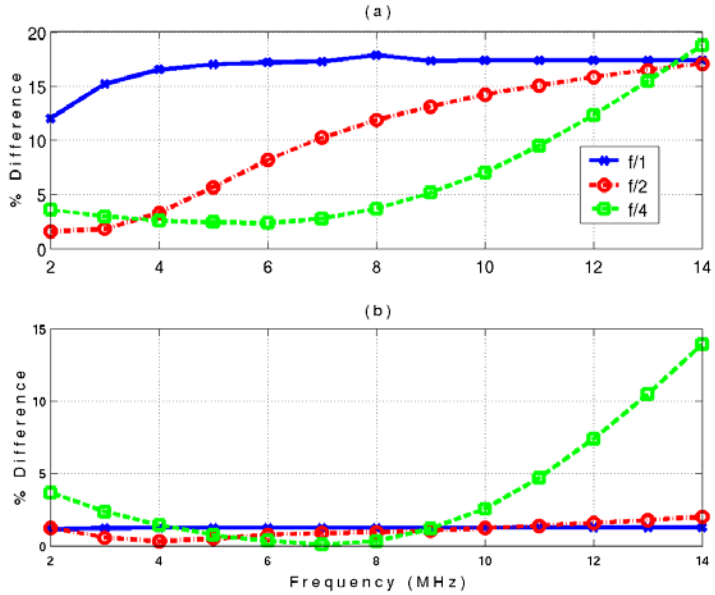

Figure E.1: The percent differences between the complete field and the Gaussian approximation for spherically focused transducers with f-numbers of 1, 2, and 4 for frequencies from 2 MHz to 14 MHz calculated using (a) Equation (E.3) and (b) Equation (E.4).

In order to investigate the errors in the approximation in greater detail, the normalized complete field intensity (i.e., $\left(\phi_{comp}(\lambda)\Big/\max_{V'}\left(\phi_{comp}(\lambda_o)\right)\right)^2$) and the accompanying Gaussian approximation were plotted for the beam axis (i.e., *z*-axis) and the beamwidth axis (i.e., r_ρ-axis) for each of the transducers for frequencies of 4 MHz, 8 MHz, and 12 MHz as shown in Figures E.2, E.3, and E.4. For all three transducers and all three frequencies, the Gaussian approximation is in good agreement with the complete field intensity along the beamwidth axis with only a slight discrepancy in the peak value for the *f*/4 transducer at 4 MHz and 12 MHz. Likewise, the agreement is good along the beam axis for the *f*/2 and *f*/1 transducers for all three frequencies as well as for the *f*/4 transducer at 8 MHz. However, the Gaussian approximation differs significantly from the complete field for the *f*/4 transducer at frequencies of 4 MHz and 12 MHz. The discrepancy for the *f*/4 transducer is due to the location of the maximum field intensity (i.e. focus) changing with transmitted frequency whereas the basic Gaussian approximation assumes

that the location is independent of frequency. The effects of the shift of the focus are more pronounced at the higher frequency (i.e., Figure E.4c) due to the smaller depth of focus.

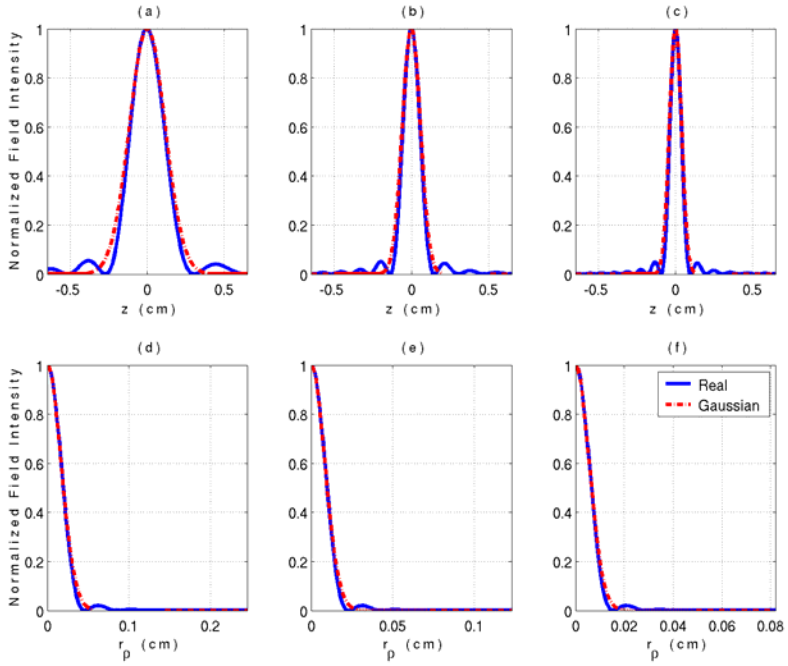

Figure E.2: Plots showing the normalized complete field intensity with the accompanying Gaussian approximation for the *z*-axis at frequencies of (a) 4 MHz, (b) 8 MHz, and (c) 12 MHz as well as the r_ρ-axis at frequencies of (d) 4 MHz, (e) 8 MHz, and (f) 12 MHz for an *f*/1 spherically focused transducer.

In addition to shifting the focus, the value of G_o, as given by Equation (2.38), also changed with frequency for the *f*/4 source. Figure E.5 shows the value of $\left(\max_{V'}\left(\phi_{comp}(\lambda)\right)\Big/\max_{V'}\left(\phi_{comp}(\lambda_o)\right)\right)^2$ (i.e., proportional to value of G_o^2 from complete source) for all of the frequencies for the calculated velocity potential field for the *f*/4 source. In addition, a line corresponding to $\left(F(8\ \text{MHz})/F(f)\right)^2$ (i.e., proportional to ideal value of G_o^2 from Equation (2.38)), where $F(f)$ is the location of the focus at each frequency, is also shown. The values of G_o^2 from the complete source follow the same trend as the ideal G_o^2 values. Also, for frequencies greater than 5 MHz for this source, the frequency dependence of G_o is not significant. Hence, the larger percent differences reported in Figure E.1 for the *f*/4 transducer at higher frequencies are due to the shifts in the location of the maximum field intensity (i.e., focus) alone.

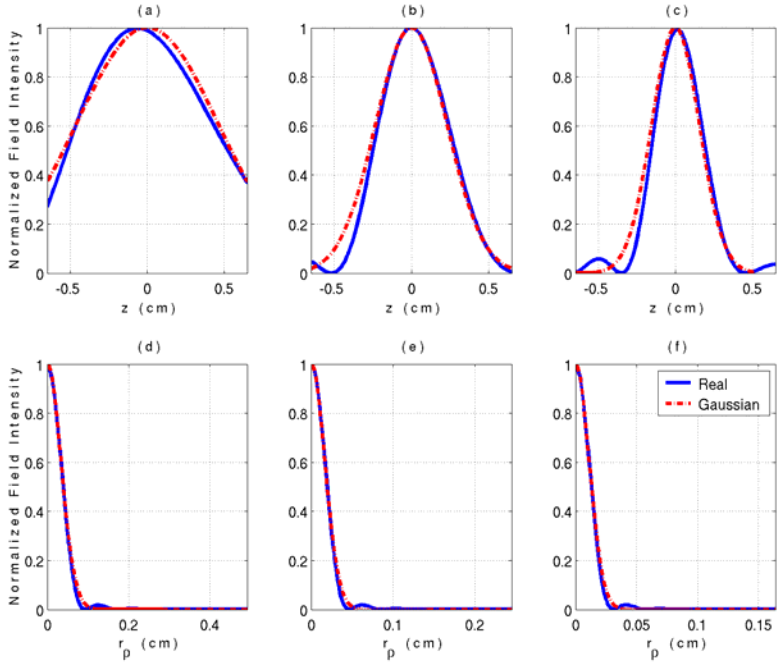

Figure E.3: Plots showing the normalized complete field intensity with the accompanying Gaussian approximation for the z-axis at frequencies of (a) 4 MHz, (b) 8 MHz, and (c) 12 MHz as well as the r_ρ-axis at frequencies of (d) 4 MHz, (e) 8 MHz, and (f) 12 MHz for an f/2 spherically focused transducer.

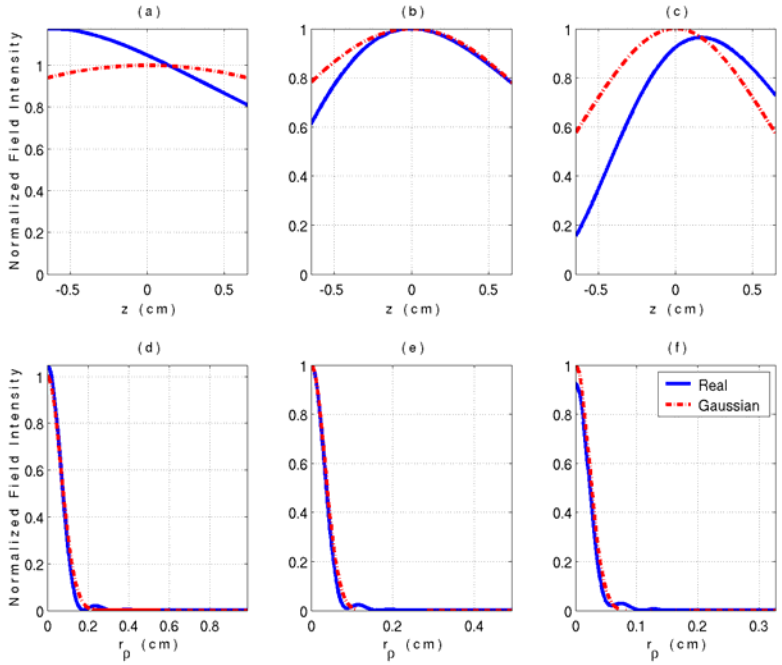

Figure E.4: Plots showing the normalized complete field intensity with the accompanying Gaussian approximation for the z-axis at frequencies of (a) 4 MHz, (b) 8 MHz, and (c) 12 MHz as well as the r_ρ-axis at frequencies of (d) 4 MHz, (e) 8 MHz, and (f) 12 MHz for an f/4 spherically focused transducer.

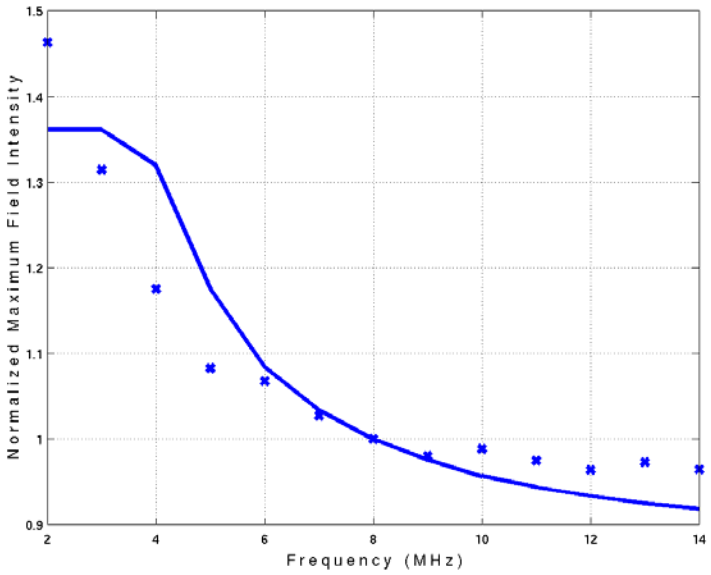

Figure E.5: Plot showing the values of G_o^2 from a complete *f*/4 source (x) normalized with respect to the complete G_o^2 at 8 MHz with a line showing the ideal values of G_o^2 from Equation (2.38) also normalized with respect to the ideal G_o^2 at 8 MHz.

Having identified the predominance of the shifts of the focus with frequency, the next step is to determine if the Gaussian approximation could be improved by properly accounting for the shift. Since the shift is always along the beam axis, Equation (2.54) could be modified to yield

$$\begin{aligned}\int_{-L/2}^{L/2} ds_z \left(g_{win}(s_z) e^{-\frac{4(s_z - z_{oF}(f))^2}{w_z^2}} e^{4\alpha_1 s_z} \right) &= \int_{-L/2}^{L/2} ds_z \left(g_{win}(s_z) e^{-\frac{4s_z^2}{w_z^2} + \frac{8 s_z z_{oF}(f)}{w_z^2} - \frac{4 z_{oF}^2(f)}{w_z^2}} e^{4\alpha_1 s_z} \right) \\ &= e^{-\frac{4 z_{oF}^2(f)}{w_z^2}} \int_{-L/2}^{L/2} ds_z \left(g_{win}(s_z) e^{-\frac{4s_z^2}{w_z^2}} e^{\left(4\alpha_1 + \frac{8 z_{oF}(f)}{w_z^2}\right) s_z} \right),\end{aligned} \tag{E.5}$$

where, in this case, z_{oF} is the shift of the focus at a particular frequency. However, the shift of the focus is typically much smaller than w_z. Hence, the terms involving z_{oF} can be ignored resulting in the same generalized attenuation-compensation function given in Equation (2.51). Therefore, the Gaussian approximation could be improved for weakly focused sources provided the equivalent Gaussian depth of focus is found by an independent fit to a Gaussian distribution for every frequency of interest while allowing the peak of the Gaussian to occur at different spatial locations for each frequency. Hence, when finding the Gaussian depth of focus for the

real sources in Chapter 3, the Gaussian fit performed allowed the focus to occur at different locations along the beam axis for each frequency.

Now that the percent differences for the weakly focused *f*/4 source have been analyzed, the percent differences for the *f*/1 and *f*/2 sources can be explored in greater detail. The calculated field intensities in dB (i.e. $10\cdot\log_{10}\left(\left(\phi_{comp}(\lambda)/\max_{V'}\left(\phi_{comp}(\lambda_o)\right)\right)^2\right)$) for the complete *f*/1 source at frequencies of 4 MHz, 8 MHz, and 12 MHz are shown with the difference term from the integrand in Equation (E.3) also in dB (i.e. $10\cdot\log_{10}\left(\left|\left(\frac{\phi_{comp}(\lambda)}{\max_{V'}\left(\phi_{comp}(\lambda_o)\right)}\right)^2-e^{-2\left(\left(\frac{r'_\rho}{w_x(\lambda)}\right)^2+\left(\frac{z'}{w_z(\lambda)}\right)^2\right)}\right|\right)$) over the integration region in Figures E.6, E.7, and E.8 respectively. Likewise, the calculated field intensities and difference term for the *f*/2 source at frequencies of 4 MHz, 8 MHz, and 12 MHz are shown in Figures E.9, E.10, and E.11, respectively.

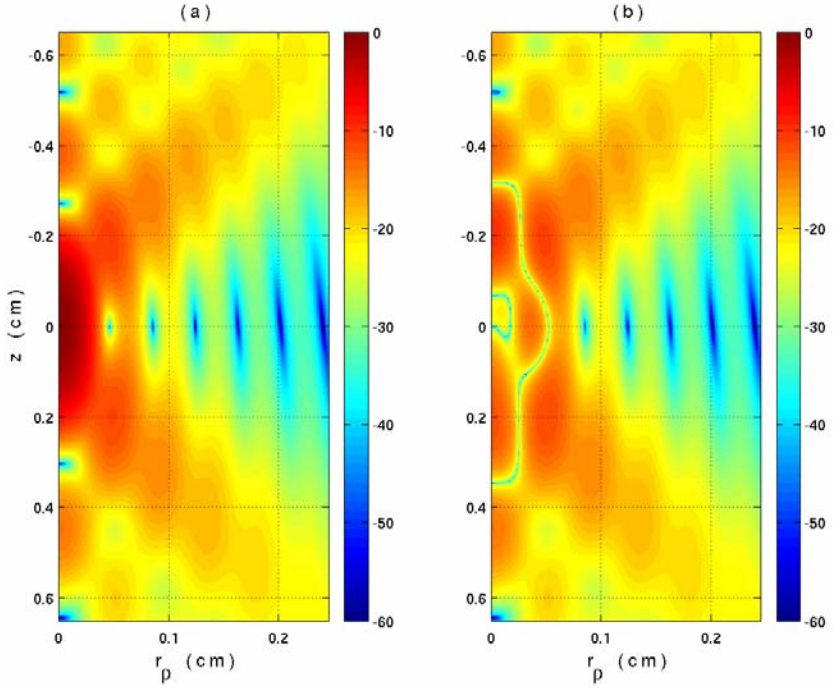

Figure E.6: Images showing (a) the calculated field intensities in dB and (b) the difference term from the integrand in Equation (E.3) also in dB for the complete *f*/1 source at a frequency of 4 MHz over the integration region.

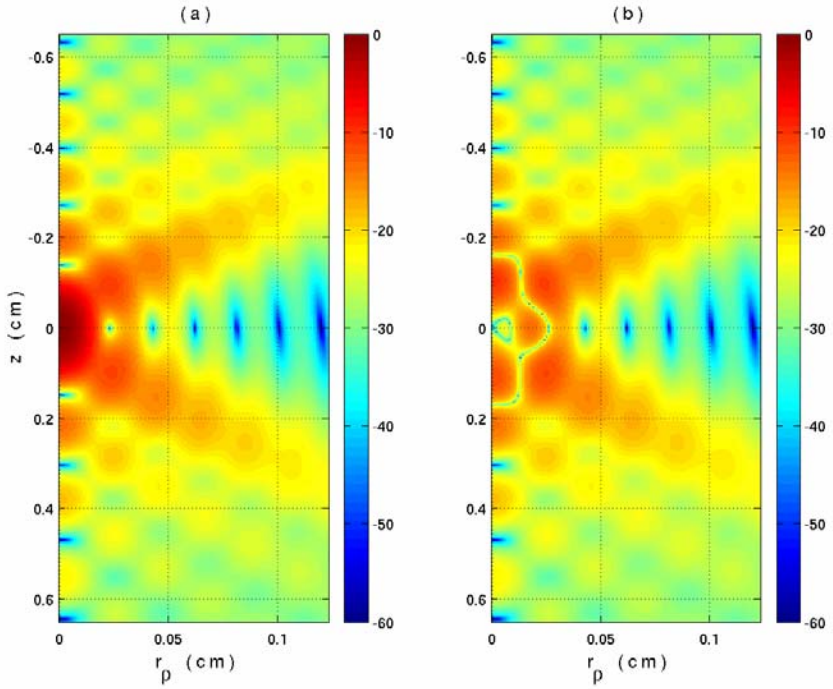

Figure E.7: Images showing (a) the calculated field intensities in dB and (b) the difference term from the integrand in Equation (E.3) also in dB for the complete *f*/1 source at a frequency of 8 MHz over the integration region.

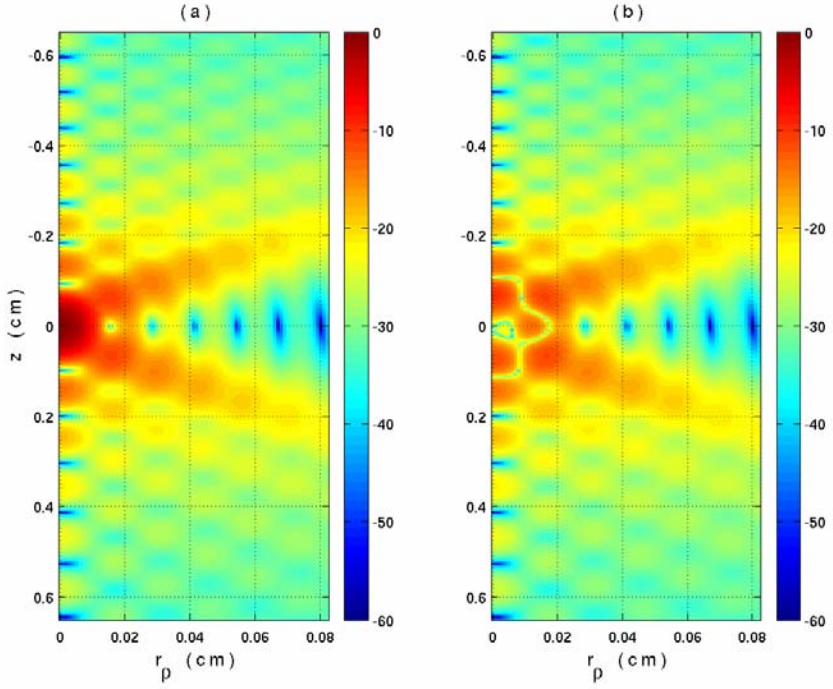

Figure E.8: Images showing (a) the calculated field intensities in dB and (b) the difference term from the integrand in Equation (E.3) also in dB for the complete *f*/1 source at a frequency of 12 MHz over the integration region.

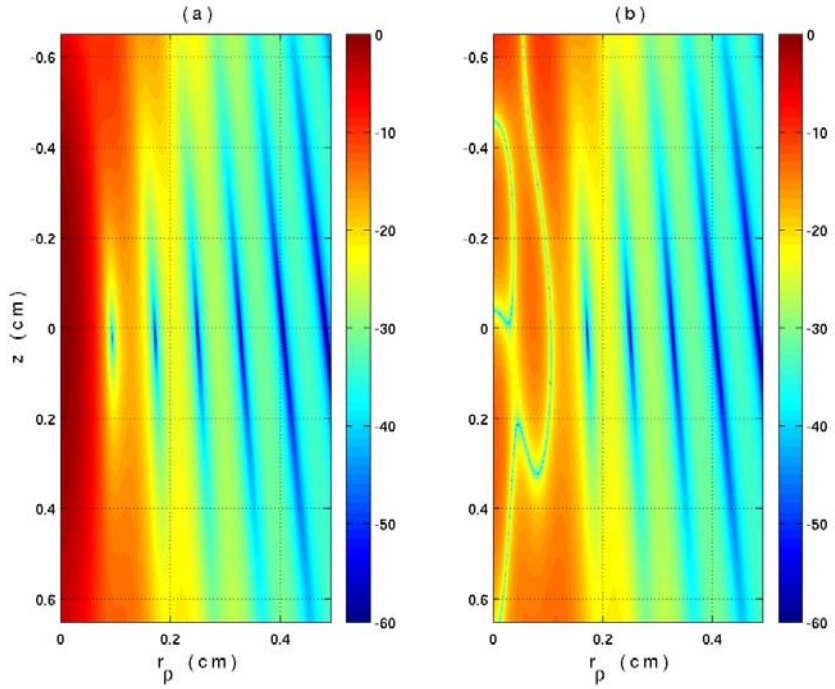

Figure E.9: Images showing (a) the calculated field intensities in dB and (b) the difference term from the integrand in Equation (E.3) also in dB for the complete *f*/2 source at a frequency of 4 MHz over the integration region.

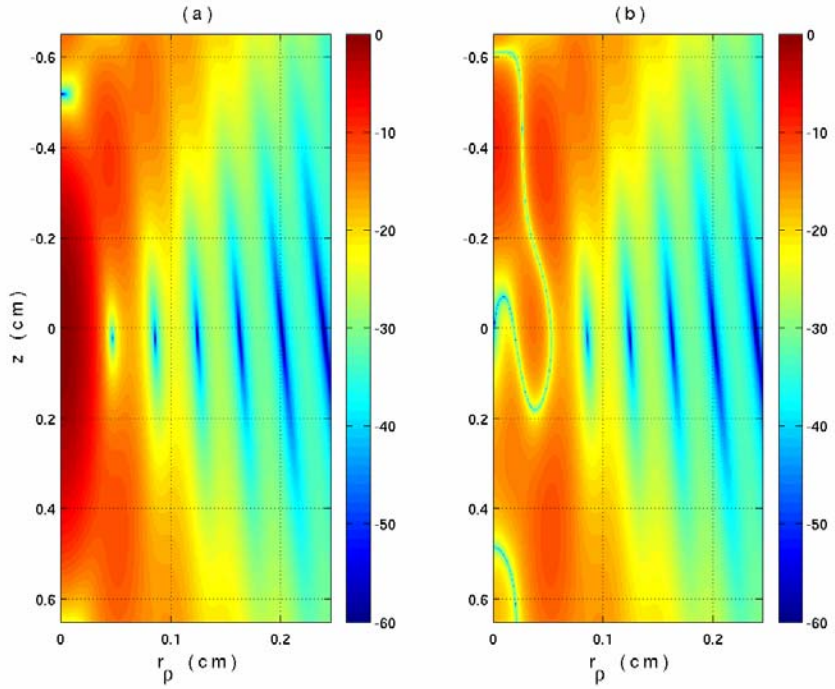

Figure E.10: Images showing (a) the calculated field intensities in dB and (b) the difference term from the integrand in Equation (E.3) also in dB for the complete *f*/2 source at a frequency of 8 MHz over the integration region.

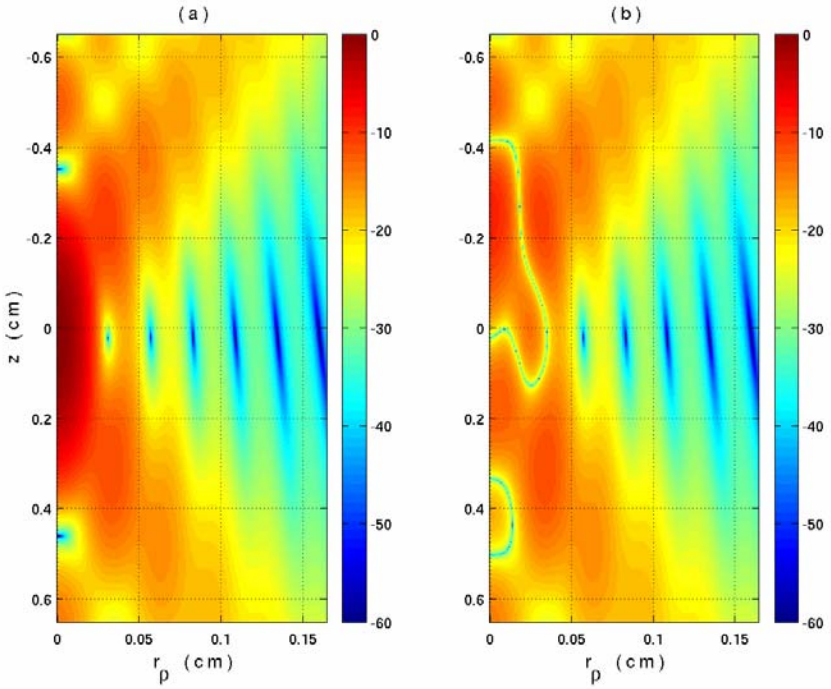

Figure E.11: Images showing (a) the calculated field intensities in dB and (b) the difference term from the integrand in Equation (E.3) also in dB for the complete *f*/2 source at a frequency of 12 MHz over the integration region.

The largest differences between the complete fields and Gaussian approximations in Figures E.6 through E.11 (i.e., (b) images) result from the "V" shaped side lobe structure before and after the focal plane. When very little of this side lobe structure is included in the integration region (Figure E.9); the corresponding percent difference in Figure E.1a is 3.3%. However, when all of the "V" is included in the integration region (Figures E.7 and E.8), the corresponding percent difference in Figure E.1a is close to 18%. Hence, the side lobe structure reduces the accuracy of the Gaussian approximation for focused sources up to a percent difference of ~18%. One way to improve the agreement between the complete fields and Gaussian approximation for focused sources is to use smaller window lengths to gate the time domain signal so that not all of the "V" shaped side lobe structure would influence the backscattered power spectrum.